Evidence of Bulk Proton Insertion in Nanostructured Anatase and Amorphous TiO_2 Electrodes

Nikolina Makivić,[ǂ] Jae-Young Cho,[¤] Kenneth D. Harris,[¤,#] Jean-Marie Tarascon,[§] Benoît Limoges,*[,ǂ] Véronique Balland*[,ǂ]

[ǂ]Université de Paris, Laboratoire d'Electrochimie Moléculaire, UMR 7591, CNRS, F-75013 Paris, France

[¤]National Research Council of Canada, Nanotechnology Research Centre, 11421 Saskatchewan Drive, Edmonton, Alberta T6G 2M9, Canada

[#]Department of Mechanical Engineering, University of Alberta, Edmonton, Alberta T6G 2V4, Canada

[§]Chimie du Solide et de l'Energie, UMR 8260, Collège de France, 11 Place Marcelin Berthelot, 75231 Paris Cedex 05, France

A- Modeling and simulations of the CVs and galvanostatic curves S1-S9

B- Supplementary Tables S10-S11

C- Supplementary Figures S12-S17

D- References S18

A - Modeling and simulations of the CVs and galvanostatic curves

I. Glossary of symbols

Latin lower case

d_f : mesoporous film thickness

d_a : compact equivalent film thickness

g : Frumkin parameter

i : current

i_f : faradaic charge storage current

i_g : galvanostatic current applied in potentiometry

i_c : capacitive current

i_H : faradaic HER current

k_{index} : rate constants

k^0 : standard heterogeneous rate constant

t : time

t_{inv} : time where the scan is inverted

t_{max} : the maximal time in potentiometry

v : scan rate in cyclic voltammetry

x : distance perpendicular to the underlying planar conductive electrode

Capital Latin

$C_{\mathrm{SUBSCRIPT}}$: volume concentration of the subscript species

$C^0_{\mathrm{SUBSCRIPT}}$: bulk material volume concentration of the subscript species

C^0_{e} : maximal concentration of electrons that can be injected in the semiconductive film

C_f : the total double layer capacitance of the film

C_{dl} : differential capacitance

$D_{\mathrm{SUBSCRIPT}}$: diffusion coefficient of the subscript species

E : potential of the electrode

E_i : initial potential

E_f : potential at scan inversion

E^0 : standard potential

E_{CB} : conduction band potential of the film

F: Faraday constant

K_a: acid dissociation constant

R: gas constant

S: geometrical electrode surface area

S_a: specific electroactive surface area

T: absolute temperature

Greek lower case

α : transfer coefficient

β : parameter characterizing the transition from the insulating to conductive state of the film

δ : a multiple of the thickness of the diffusion-natural convection layer

θ : film state-of-protonation

II. Model

The model is similar to our previous publication.[1] Briefly, the porous semi-conductive TiO_2 film (defined by a thickness d_f and an accessible specific solid surface area S_a), deposited over a flat and inert conductor of geometric surface area S, is assimilated to a flat compact film of thickness d_a and accessible surface S_a. The migration of protons within the solid phase is assumed to follow a linear finite diffusion, occurring normal to the metal oxide/electrolyte interface. Outside the film, the diffusion of soluble species in the electrolyte is also considered to be linear but semi-infinite toward a surface area S (Scheme S1). This modeling simplification is valid if the constrained diffusion within the pores is assumed to be negligible, which is valid here considering the relatively large and opened porosity of the nanostructured GLAD TiO_2 film. This allows for fast diffusion of the electrolyte species throughout the film. The model also assumes a homogeneous distribution of immobile redox units O (*i.e.*, $Ti^{IV}O_2$) that are able to be reduced into immobile RH units (*i.e.*, $Ti^{III}OOH$) within the bulk film (with a total volumetric concentration C_O^0 of redox-active units). For all species, activities will be assimilated to concentrations in the following.

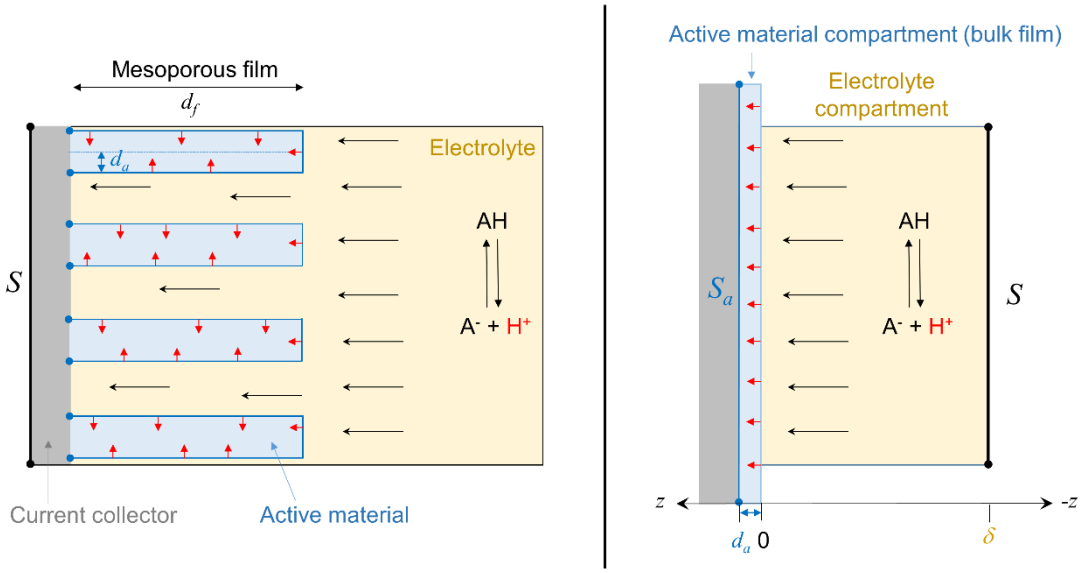

Scheme S1. Schematic representation of the (left) mesoporous GLAD TiO_2 electrode and (right) its two-compartment simplified model. The black arrows symbolize the directional mass transport of AH during electrode reduction, while the red arrows symbolize the concomitant solid-state mass transport of inserted protons.

On the basis of this simplified two-compartment model, the accessible film thickness for proton diffusion in the bulk film (*i.e.*, $0 < z < d_a$, corresponding to the active material compartment) along the *z*-axis (the origin of which is defined at the active material/electrolyte interface) can be estimated from the following mole conservation law:

$$C_{\mathrm{O}}^{0} S_a d_a = (1-p)\, x C_{\mathrm{O}}^{0,tot} S d_f \qquad \text{(S1)}$$

where p is the porosity of the mesoporous film (*i.e.*, the ratio of the void volume to the geometric volume $S \times d_f$) and x is a stoichiometric factor indicating the fraction of immobile redox-active units (*i.e.*, $x = C_{\mathrm{O}}^{0} / C_{\mathrm{O}}^{0,tot}$).

Electrolyte compartment ($z < 0$)

Outside the film, the electrolyte compartment is filled with a buffered aqueous electrolyte consisting of a mixture of proton donor AH, proton acceptor A^-, and free protons H^+, which diffuse normal to the electrode (linear semi-infinite diffusion) with diffusion coefficients D_{AH}, $D_{\mathrm{A^-}}$, and $D_{\mathrm{H^+}}$, respectively. The concentrations C_{AH}, $C_{\mathrm{A^-}}$ and $C_{\mathrm{H^+}}$ rapidly equilibrate according to the following acid-base equilibrium:

$$\mathrm{AH} \underset{k_-}{\overset{k_+}{\rightleftarrows}} \mathrm{A^-} + \mathrm{H^+}$$

The equilibrium is characterized by a thermodynamic equilibrium constant: $K_A = \dfrac{k_+}{k_-} = \dfrac{C_{\mathrm{A^-}} C_{\mathrm{H^+}}}{C_{\mathrm{AH}}} = 10^{-pH} \dfrac{C_{\mathrm{A^-}}}{C_{\mathrm{AH}}}$.

For the electrolyte compartment, we can thus write the following three coupled diffusion-reaction differential equations:

$$\frac{\partial C_{\mathrm{AH}}}{\partial t} = D_{\mathrm{AH}} \frac{\partial^2 C_{\mathrm{AH}}}{\partial z^2} + k_+ C_{\mathrm{A^-}} C_{\mathrm{H^+}} - k_- C_{\mathrm{AH}} \qquad \text{(S2)}$$

$$\frac{\partial C_{A^-}}{\partial t} = D_{A^-}\frac{\partial^2 C_{A^-}}{\partial z^2} - k_+ C_{A^-} C_{H^+} + k_- C_{AH} \quad \text{(S3)}$$

$$\frac{\partial C_{H^+}}{\partial t} = D_{H^+}\frac{\partial^2 C_{H^+}}{\partial z^2} - k_+ C_{A^-} C_{H^+} + k_- C_{AH} \quad \text{(S4)}$$

Film compartment ($0 < z < d_a$)

Within the active material compartment, the inserted protons at the solid/electrolyte interface migrate across the solid phase through a H-atom hopping process equivalent to a diffusion-like process (finite linear diffusion), the rate of which can be described by the following derivative equations specifying the solid-state concentrations of O and RH:

$$\frac{\partial C_O}{\partial t} = D_{H,in}\frac{\partial^2 C_O}{\partial z^2} \quad ; \quad \frac{\partial C_{RH}}{\partial t} = D_{H,out}\frac{\partial^2 C_{RH}}{\partial z^2} \quad \text{(S5)}$$

where $D_{H,in}$ and $D_{H,out}$ are the apparent solid-state diffusion coefficients of protons during the reduction (*i.e*, insertion) and oxidation (*i.e.*, disinsertion) steps of the metal oxide film, respectively. As we will see, their values are not necessarily identical.

Note that because the film is electronically conductive when protons are inserted, we can consider a uniform potential across the bulk film and also assume that there is no potential drop at the film/underlying electrode interface**.**

III. Boundary conditions at the solution-film interface (source terms at z = 0)

a- Faradaic charge storage reaction

At the solution-film interface, proton insertion/disinsertion occurs through the following reversible proton-coupled electron transfer reaction:

$$O + AH + e^- \rightleftharpoons RH + A^-$$

characterized by the standard potential E^0 of the (O+AH)/(RH+A^-) proton-coupled electron transfer couple, k^0 the standard heterogeneous rate constant of the process, and α the transfer coefficient. The kinetics of this interfacial electrochemical insertion reaction can be described using the Butler-Volmer formalism for a concerted process, modified by a Frumkin-type energetic term in

such a way to take into account the non-ideality resulting from the interaction energy between the intercalation sites in the host matrix, *i.e.*:

$$\frac{i_f}{FS_a} = D_{\mathrm{H,in}}\left(\frac{\partial C_{\mathrm{O}}}{\partial z}\right)_{z=0}$$
$$= k^0 \exp\left[\alpha g \frac{(C_{\mathrm{O}})_{z=0}}{C_{\mathrm{O}}^0}\right]\exp\left[-\frac{\alpha F\left(E-E^0\right)}{RT}\right]\left\{\begin{array}{l}(C_{\mathrm{O}})_{z=0}(C_{\mathrm{AH}})_{z=0} \\ -(C_{\mathrm{RH}})_{z=0}\left(C_{\mathrm{A}^-}\right)_{z=0}\exp\left[-g\frac{(C_{\mathrm{O}})_{z=0}}{C_{\mathrm{O}}^0}\right]\exp\left[\frac{F\left(E-E^0\right)}{RT}\right]\end{array}\right\} \quad \text{(S6)}$$

where i_f is the faradaic current generated by the proton-coupled electron transfer reaction and g is a dimensionless constant characterizing the mean interaction energy between intercalation sites (positive for repulsion and negative for attraction).

The state-of-protonation of the film being given by $\theta = C_{\mathrm{RH}}/C_{\mathrm{O}}^0 = \left(C_{\mathrm{O}}^0 - C_{\mathrm{O}}\right)/C_{\mathrm{O}}^0$, eq S6 can thus be rewritten as follows:

$$\frac{i_f}{FS_a} = k^0 C_{\mathrm{O}}^0 \exp\left[\alpha g(1-\theta)_{z=0}\right]\exp\left[-\frac{\alpha F\left(E-E^0\right)}{RT}\right]\left\{\begin{array}{l}(1-\theta)_{z=0}(C_{\mathrm{AH}})_{z=0} \\ -(\theta)_{z=0}\left(C_{\mathrm{A}^-}\right)_{z=0}\exp\left[-g(1-\theta)_{z=0}\right]\exp\left[\frac{F\left(E-E^0\right)}{RT}\right]\end{array}\right\} \quad \text{(S7)}$$

It is worth noting that the standard potential of the (O+AH)/(RH+A^-) couple is linked to the standard potential of the O/RH couple through the pK_a of the AH/A^- couple according to:

$$E^0 = E^0{}_{\mathrm{O/RH}} - 2.302\frac{RT}{F}pK_a$$

b- Competitive hydrogen evolution reaction (HER)

In the case where it is necessary to consider the additional faradaic contribution arising from competitive hydrogen evolution at the TiO_2/electrolyte interface, the following electrochemical reduction of AH to H_2 has to be taken into account at the boundary solution-film interface:

$$\mathrm{AH} + \mathrm{e}^- \rightarrow \mathrm{A}^- + \tfrac{1}{2}\mathrm{H}_2$$

On account of the irreversibility of this process at the TiO_2 electrode and of its dependency on the AH concentration, we have assumed it can be roughly described by the following empirical rate:[2]

$$\frac{i_H}{FS} = -D_{\mathrm{AH}}\left(\frac{\partial C_{\mathrm{AH}}}{\partial z}\right)_{z=0} = -k_H^0 \left(C_{\mathrm{AH}}\right)_{x=0}^{\nu} \exp\left[-\frac{\alpha_H F\left(E - E_{eq,H}\right)}{RT}\right] \qquad \text{(S8)}$$

where k_H^0, ν, α_H, and $E_{eq,H}$ are respectively a potential-independent heterogeneous rate constant, the reaction order in proton donor, the experimental transfer coefficient, and the equilibrium potential of the HER reaction. As we will see for the simulations, we have arbitrary used a value of 1 and 0.5 for ν and α_H, respectively.

c- Double layer electrical capacitance

An additional source term that needs to be included at $x = 0$ is the capacitive current (i_c) resulting from both the charging and discharging of the double layer capacitance ($C_f = C_{dl} \times S_a$, with C_f the total double layer capacitance of the film and C_{dl} the differential capacitance). This capacitive current is generated from ionic adsorption over the specific surface area of the TiO_2 film (mainly involved when TiO_2 behaves as a metal-like conductor, *i.e.* at $E < E_{CB}$) and the exponential filling/emptying of the chemical capacitance (C_{chem}) associated with the transition from an insulating to a conductive state (i.e., a doping process which arises through the injection of electrons from the underlying conductor into the conduction band as well as bandgap localized states of TiO_2).[3] The total capacitive current is in fact electrically equivalent to the charging/discharging of two capacitances in series, one being independent of potential, *i.e.* $C_{dl} \times S_a$, and the other being an exponential function of potential according to: $C_{chem} = \frac{\beta F^2}{RT} d_f C_e^0 \exp\left[-\beta \frac{F}{RT}\left(E - E_{CB}\right)\right]$ (where β is a thermodynamic parameter reflecting the energetic distribution of the conduction states of TiO_2 and C_e^0 the maximal volumetric concentration of electrons that can be injected into semiconductive film).[4] E_{CB} is the conduction band potential of TiO_2, with pH-dependence given by the following expression: $E_{CB} = E_{CB}^0 - \frac{RT}{F} pH$ where E_{CB}^0 is the corresponding standard (*i.e.*, pH = 0) conduction band potential.[5]

Assuming that the charge/discharge of the double-layer and chemical capacitances are almost instantaneous, we can thus apply the following source term for the capacitive current at the boundary solution-film interface:

$$\frac{i_C}{FS} = \frac{1}{\frac{1}{C_{dl}S_a} + \frac{1}{C_{chem}}} \left(\frac{\partial E}{\partial t}\right)_{z=0} \quad \text{(S9)}$$

d- Electrode self-discharge

A final contribution that also had to be taken into account in the model is the self-discharge of the protonated film. This was indeed observed to interfere in the galvanostatic experiments carried out at slow rates. We assumed that this self-discharge could be formally described by the spontaneous surface recombination of two inserted protons, leading to the release of H_2:

$$2\,\mathrm{RH} \xrightarrow{k_{self}} 2\,\mathrm{O} + \mathrm{H_2}$$

where k_{self} is the rate constant of the reaction. The flux of this reaction at $z = 0$ can thus be defined by:

$$-D_{\mathrm{H,out}} \left(\frac{\partial C_{\mathrm{RH}}}{\partial z}\right)_{z=0} = -2k_{self} \left(C_{\mathrm{RH}}\right)^2_{z=0}$$

IV. Initial and additional boundary conditions

$t = 0,\ 0 < z < d_a:\ C_{\mathrm{O}} = C^0_{\mathrm{O}}$ and $C_{\mathrm{RH}} = 0$

$t = 0,\ z < 0$ and $z = \infty,\ \forall t: C_{\mathrm{A^-}} = C^0_{\mathrm{A^-}},\ C_{\mathrm{AH}} = C^0_{\mathrm{AH}}$, and $C_{\mathrm{H^+}} = K_A \frac{C^0_{\mathrm{AH}}}{C^0_{\mathrm{A^-}}} = C^0_{\mathrm{H^+}}$

($C^0_{\mathrm{A^-}}$, C^0_{AH}, and $C^0_{\mathrm{H^+}}$ being the bulk concentrations of each buffer species in the electrolyte).

$t > 0,\ z = 0$:

$$S_a D_{\mathrm{H,in}} \left(\frac{\partial C_{\mathrm{O}}}{\partial z}\right)_{z=0} = -S_a D_{\mathrm{H,out}} \left(\frac{\partial C_{\mathrm{RH}}}{\partial z}\right)_{z=0} = SD_{\mathrm{AH}} \left(\frac{\partial C_{\mathrm{AH}}}{\partial z}\right)_{z=0} = -SD_{\mathrm{A^-}} \left(\frac{\partial C_{\mathrm{A^-}}}{\partial z}\right)_{z=0} \quad \text{(S10)}$$

$t > 0,\ z = d_a$:

$$\left(\frac{\partial C_{\mathrm{O}}}{\partial z}\right)_{z=d_a} = -\left(\frac{\partial C_{\mathrm{RH}}}{\partial z}\right)_{z=d_a} = 0$$

Cyclic voltammetry conditions

$0 < t < t_{inv} : E = E_i - vt$

$t_{inv} < t < 2t_{inv} : E = E_f + vt$

Expression of the current

The total current is given by the sum of the faradaic and capacitive contributions, *i.e.* $i_t = i_C + i_f + i_H$, while the faradaic charge-storage current is evaluated as proportional to the sum of all oxidized species in the film being reduced by unit of time:

$$\frac{i_f}{FS_a} = -\int_0^{d_a} \frac{\partial C_O}{\partial t} dz \qquad \text{(S12)}$$

V. Procedure for numerical calculation

The above model was numerically simulated by finite element analysis using COMSOL Multiphysics (v. 5.5) software, with both electroanalysis and mass transport of diluted species modules, on a PC computer with Intel Core i5 CPU and 8 GB RAM, and Windows 10 operating system. The 1D simulation geometry in the *z*-direction was as per the schematic in Scheme S1 (bottom of the left representation) based on two joint interval domains, one defined by the film dimension d_a and the other by the distance δ in the electrolyte. The latter was selected as a multiple of the diffusion layer thickness ($\sqrt{Dt}$) in order to avoid alteration of the bulk concentrations. Direct PARDISO solver with a relative tolerance of 10^{-5} was used in the software. The maximal element size was 10^{-5} μm in the film domain and 2 μm in the electrolyte domain. A meshing refinement was also applied to the overall geometry, and the time steps were controlled by the software. In order to include the influence of the natural convection that mainly takes place at slow rates, an *x*-vector velocity field of -8×10^{-6} m/s was systematically applied to the simulations (a value which allows us to restrict the growth of the diffusion layer to a maximal thickness of ~200 μm). The Ohmic drop in the simulations was obtained

by setting the film conductivity to a constant value of 1.2×10^{-5} S/cm, which is equivalent to an Ohmic drop of 8 Ω/cm^2.

B - Supplementary Tables

Table S1. Set of adjusted parameters used in the model to simulate the CVs reported in Figures S1, 2 and 3.

	Associated parameters	Amorphous	Anatase	Nafion-coated anatase
Bulk film compartment	d_a (nm)	**1.22**	**4.26**	**4.26**
	S_a/S	**540**	**155**	**155**
	C_O^0 (M)	24	24	24
Proton de(insertion) reaction	k^0 (cm^4·mol·s)	**5 × 10^6**	**20 × 10^6**	**5 × 10^6**
	α	0.5	0.5	0.5
	$E^0_{TiO_2/TiOOH}$ (V)	-0.7	-0.7	-0.7
	g	**16**	**-3**	**-3**
	$D_{H,in}$ (cm^2·s^{-1})	2 × 10^{-15}	2 × 10^{-15}	2 × 10^{-15}
	$D_{H,out}$ (cm^2·s^{-1})	**2 × 10^{-15}**	**8 × 10^{-15}**	**8 × 10^{-15}**
Competitive HER	k_H^0 (cm·s^{-1})	3 × 10^{-15}		
	ν	1		
	α_H	0.5		
	$E_{eq,H}$ (V)	-0.28		
Capacitance	β	0.2	0.2	0.2
	E^0_{CB} (V)	**0.02**	**-0.12**	**-0.12**
	C_e^0 (mM)	70	70	70
	C_{dl} (μF·cm^{-2})	33	33	33
Self-discharge	k_{self} (cm^4·mol·s)	10^{-9}		

Parameters differing between the TiO_2 phases are highlighted in bold. All potentials are given in V *vs.* NHE. The parameters describing the 1 M buffered electrolyte compartment were for all simulations as follows (with AH = CH_3COOH and A^- = CH_3COO^-): $D_{AH} = D_{A^-} = 4.5 \times 10^{-6}$ cm^2·s^{-1}, $D_{H^+} = 9.5 \times$

10^{-5} $cm^2 \cdot s^{-1}$,[S6] $pK_a = 4.76$, $C^0_{AH} + C^0_{A^-} = 1$ M, $C^0_{H^+} = 10^{-5}$ M, $k_+ = 10^9$ $M^{-1} \cdot s^{-1}$, and $k_- = k_+ K_a = 2433$ s^{-1}.[1]

Table S2. Electrochemical features of pure anatase TiO_2 electrodes regarding the reversible insertion of Li^+ from organic electrolytes or reversible insertion of H^+ from an aqueous electrolyte.

Film morphology	Inserting cation	ΔE_p (V) [a] in CV at 1 mV/s	Ref
Nanoparticles	Li^+	0.26	7
Nanotubes	Li^+	0.31	8
Nanotubes	Li^+	~0.5	9
Dense film on 3D substrate	Li^+	~0.65	10
Dense film	Li^+	0.57	11
Nanocolumns	H^+	0.1	This work
Nanocolumns	Li^+	0.35	This work

[a] Peak-to-peak potential difference recorded by cyclic voltammetry at 1 mV/s

C - Supplementary Figures

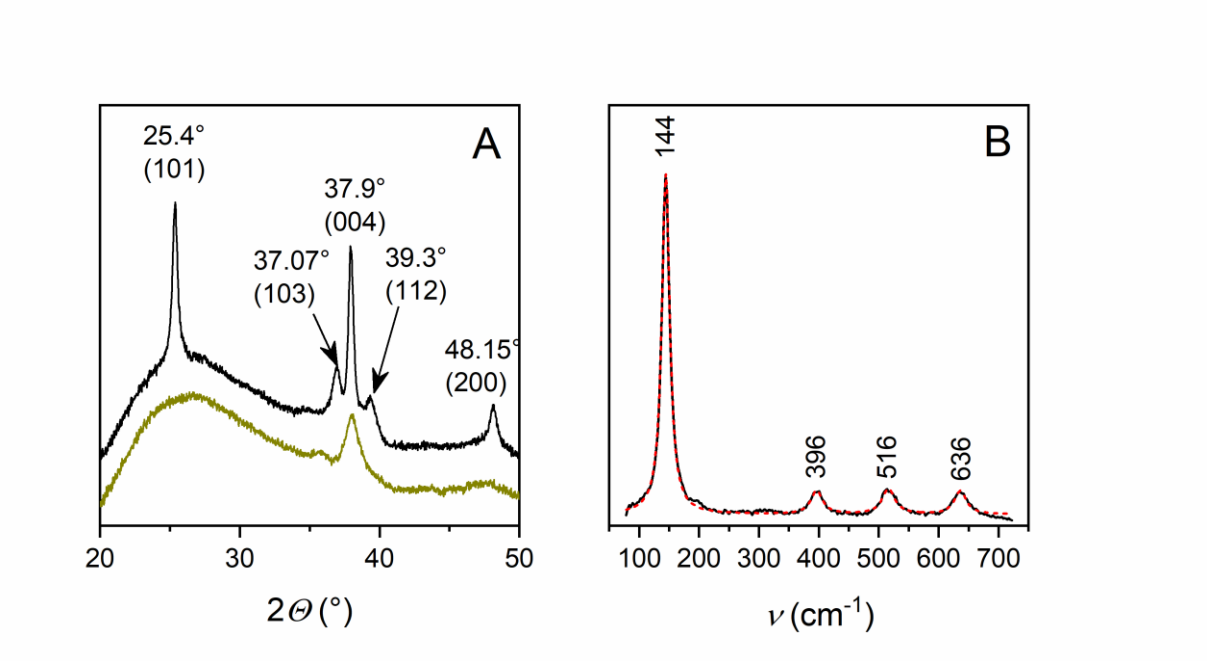

Figure S1. (A) X-Ray diffraction spectrum and (B) Raman spectrum recorded at (black lines) GLAD-TiO_2 films after thermal annealing and compared to the unannealed film (dark yellow lines in A). The Raman spectrum was fitted with a Lorentz oscillator (red dashed line).

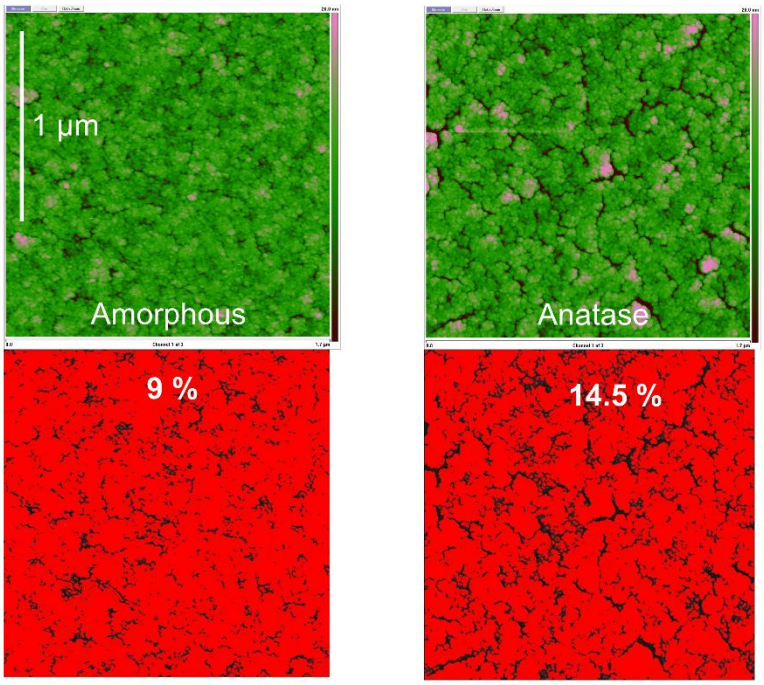

Figure S2. (green) Nano-AFM mapping of the top surface of a GLAD-TiO_2 film (left) prior to and (right) after thermal annealing with the corresponding (red) threshold-processed images highlighting the gaps between GLAD posts. The fraction of gaps are noted as insets in the lower images.

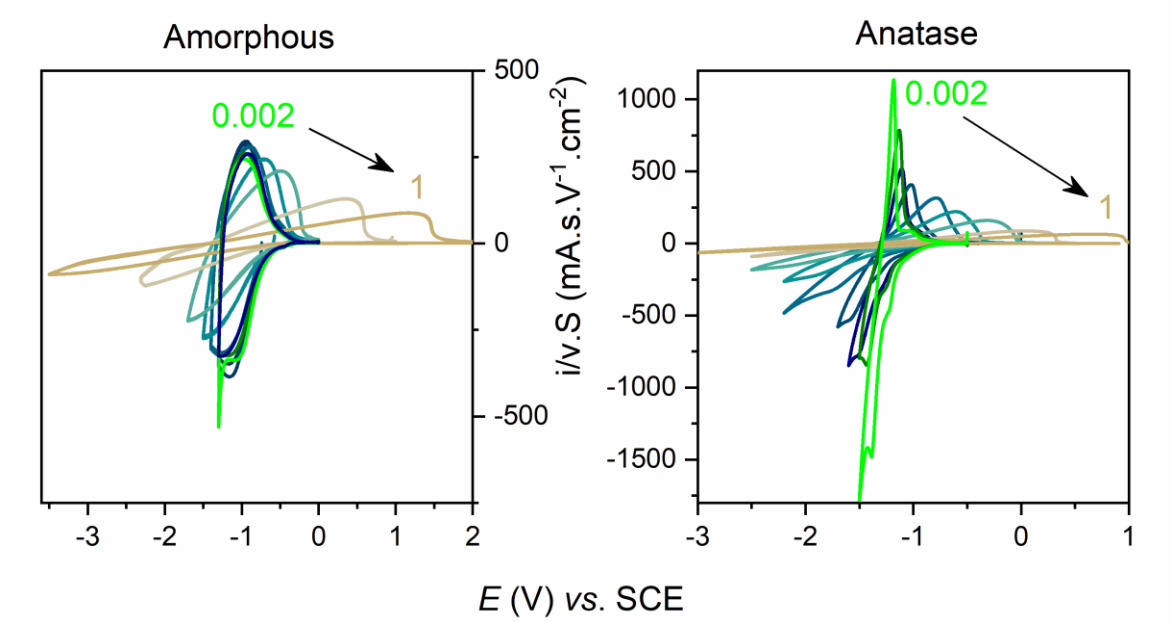

Figure S3. CVs recorded at (left) an amorphous and (red) an anatase GLAD-TiO_2 electrode in a 1 M acetate buffer electrolyte (pH 5) at various scan rates *v* (from light green to sand): 0.002, 0.005, 0.01, 0.02, 0.05, 0.1, 0.2, 0.5 and 1 V/s. For better visualization of the scan rate dependence, the current was normalized to *v*.

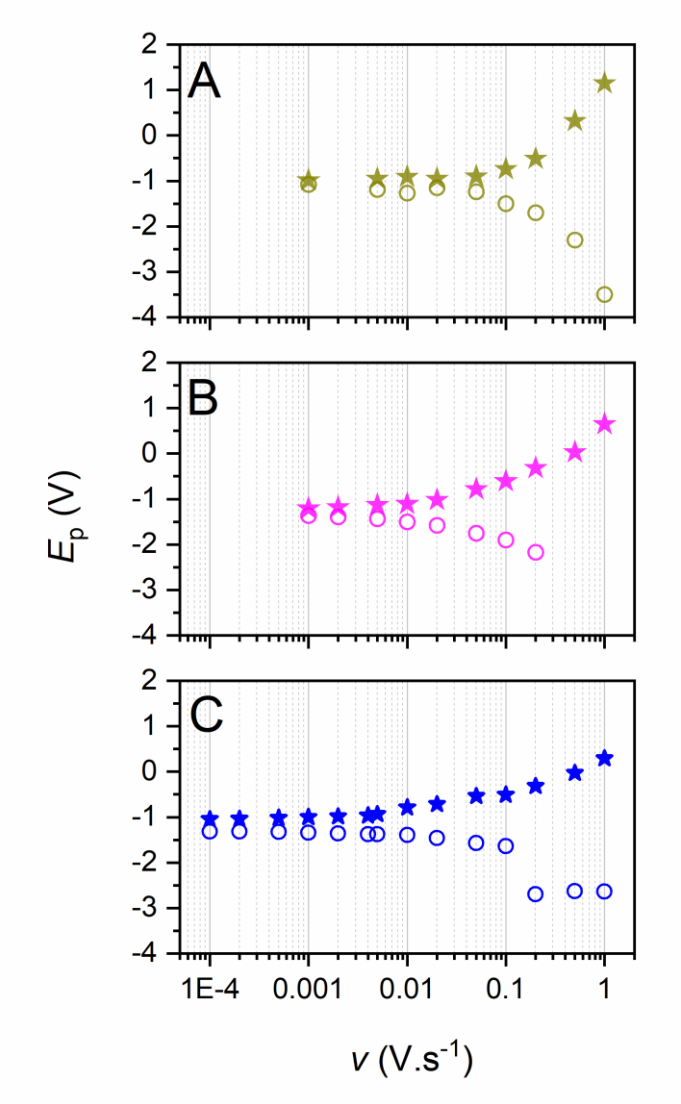

Figure S4. Influence of the scan rate on the value of the potentials of anodic and cathodic faradaic peaks (E_p) recorded by CV at (A) amorphous and (B, C) anatase GLAD-TiO_2 electrodes in (A, B) 1 M acetate buffer aqueous electrolyte or (C) 1 M $LiClO_4$ acetonitrile electrolyte.

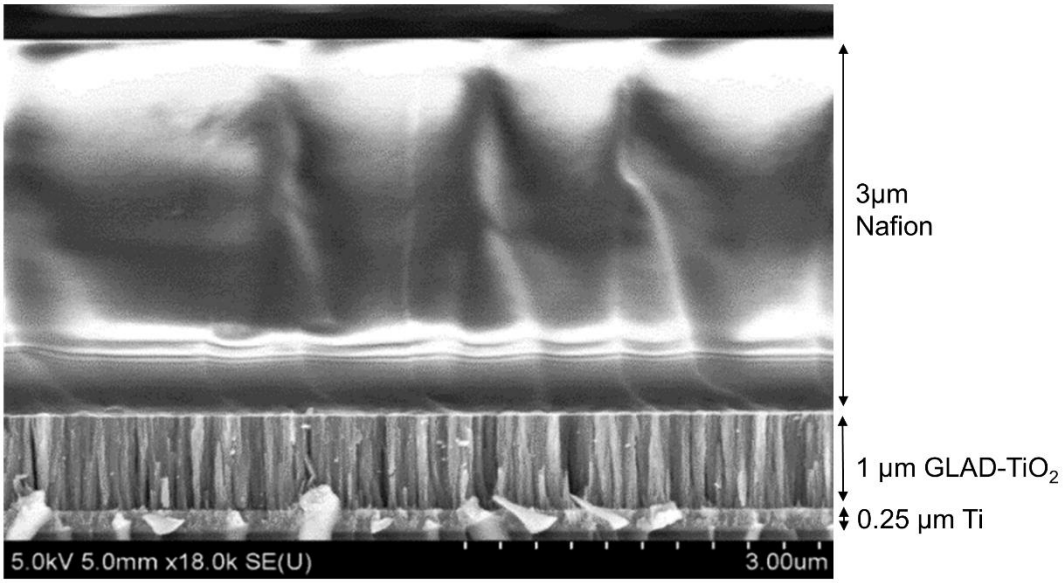

Figure S5: Cross-sectional SEM image of an amorphous GLAD-TiO_2 electrode covered by a ca. 3-µm Nafion film.

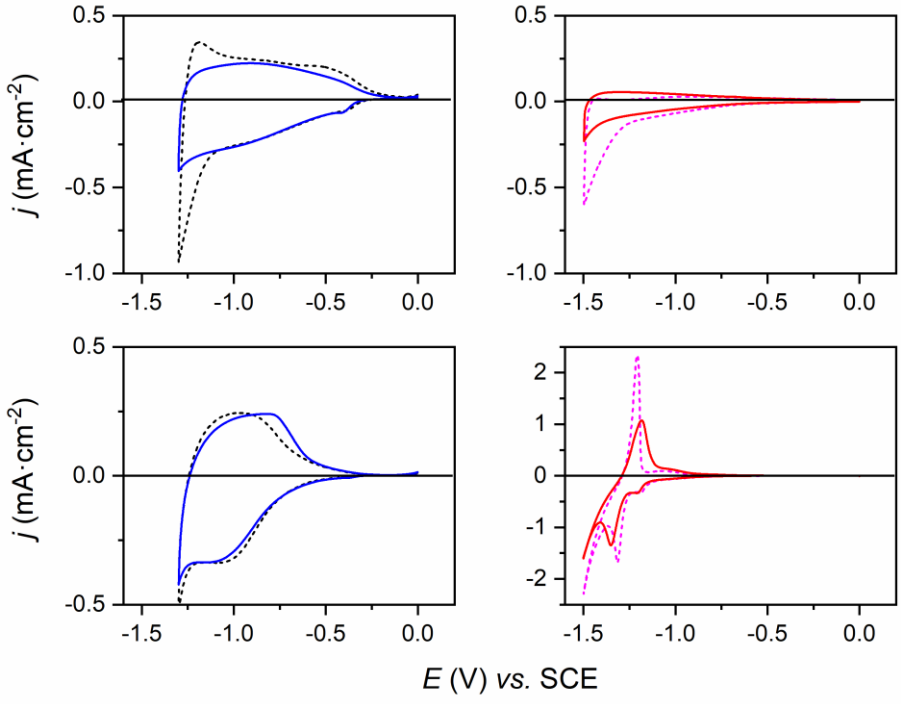

Figure S6: CVs recorded at (left) amorphous and (right) anatase GLAD-TiO_2 electrodes (top) in a 0.5 M KCl electrolyte at 10 mV/s and (bottom) in a 1 M acetate buffered electrolyte at 1 mV/s. The solid and dashed curves correspond to the CVs performed with and without a Nafion-film coating, respectively, over the nanostructured TiO_2 electrode.

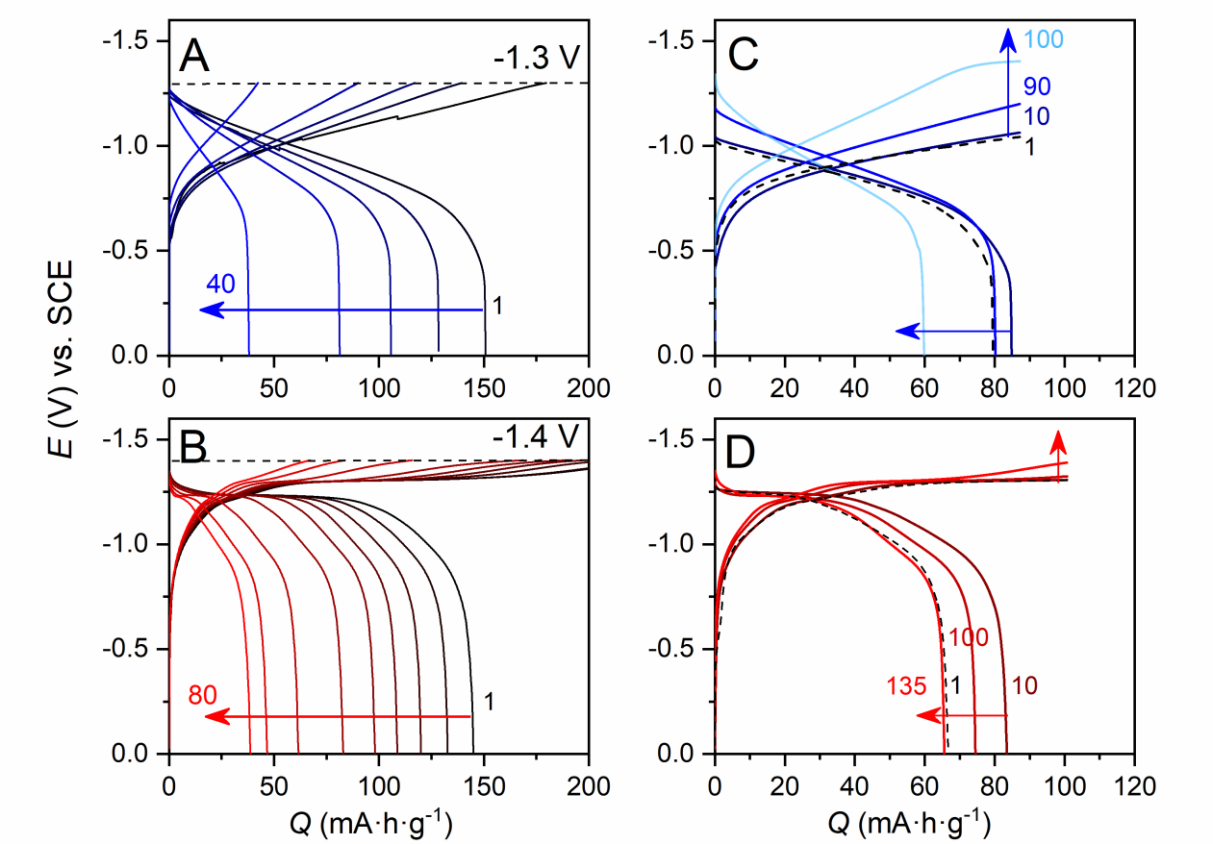

Figure S7. Continuous galvanostatic cycling experiments performed at Nafion-coated (blue) amorphous and (red) anatase GLAD-TiO_2 electrodes in a 1 M acetate buffer (pH 5). In (A) and (B), the galvanostatic charge/discharge curves (only one cycle out of ten is shown) were obtained under strong accumulation conditions using a negative cut-off potential of (A) -1.3 V for the amorphous electrode and (B) -1.4 V for the anatase electrode. In (C) and (D), the galvanostatic cycles were performed under mild accumulation conditions using a constant charge of 100 $mA \cdot h \cdot g^{-1}$ with a discharge controlled by a positive cut-off potential of 0.0 V (the first cycle is represented by the dashed black curves and the numbers on each curves indicate the cycle number). All experiments were performed at a rate of 0.36 $mA \cdot cm^{-2}$.

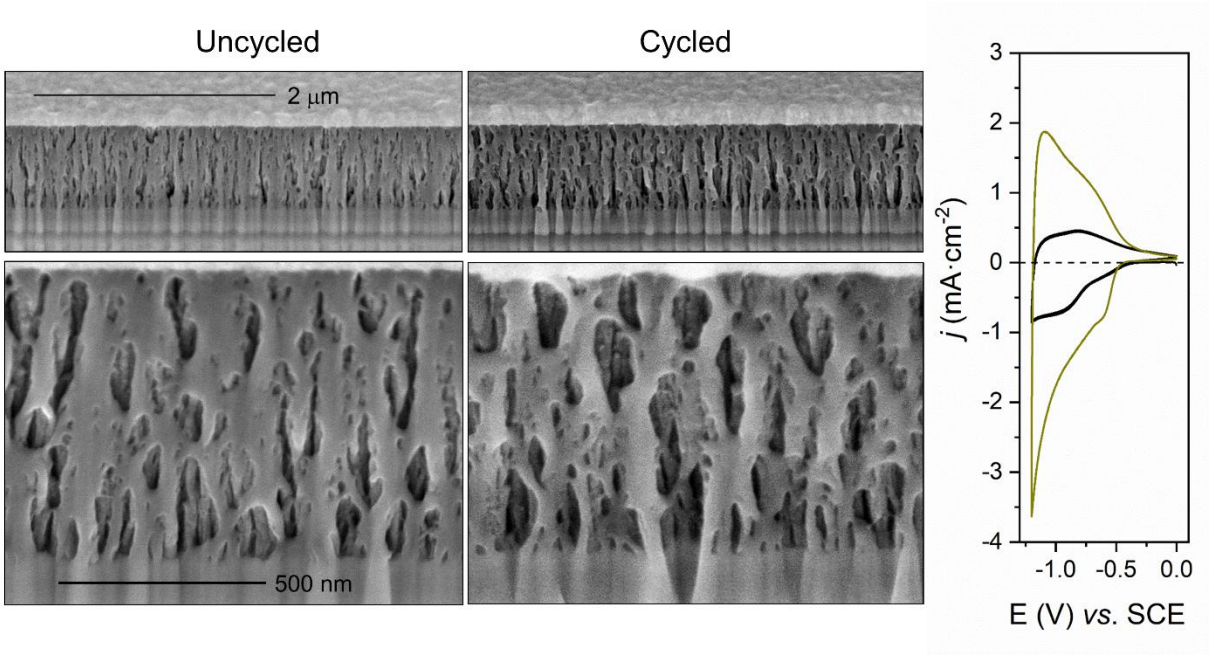

Figure S8. FIB-cross sectional images and CVs recorded at an (left images and dark yellow CV) uncycled and (right images and black CV) cycled amorphous GLAD-TiO_2 electrode. The outermost layer of TiO_2 structures have been deformed under the influence of the focussed ion beam. The galvanostatic cycling of the electrode was performed under strong accumulation conditions in a 1 M acetate buffer (pH 5) and at a rate of 1 $mA \cdot cm^{-2}$, until the discharge gravimetric capacity of the electrode was decreased by 40% (equivalent to ~10 cycles). The CVs were recorded in a 0.5 M KCl aqueous electrolyte (pH 5) at 0.1 V/s.

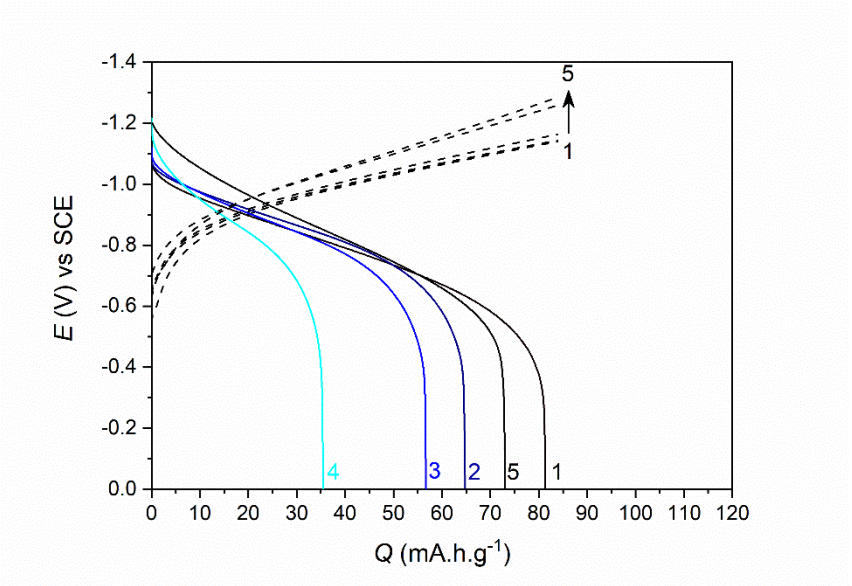

Figure S9. Continuous galvanostatic cycles performed at an amorphous GLAD-TiO_2 electrode using a rate of 5.6 $A \cdot g^{-1}$ to charge the electrode to a constant value of 80 $mA \cdot h \cdot g^{-1}$. Various discharge rates were used, all with a positive cut-off potential of 0.0 V. The numbers on the curves indicate the cycle number associated with the following discharge rate: (1, black) 5.6 $A \cdot g^{-1}$, (2, navy) 0.07 $A \cdot g^{-1}$, (3, blue) 0.03 $A \cdot g^{-1}$, (4, cyan) 0.015 $A \cdot g^{-1}$, and (5, black) 5.6 $A \cdot g^{-1}$.

D – References

(1) Kim, Y. S.; Balland, V.; Limoges, B.; Costentin, C. Cyclic Voltammetry Modeling of Proton Transport Effects on Redox Charge Storage in Conductive Materials: Application to a TiO_2 Mesoporous Film. *Phys. Chem. Chem. Phys.* **2017**, *19* (27), 17944–17951. https://doi.org/10.1039/C7CP02810E.

(2) Jackson, M. N.; Surendranath, Y. Donor-Dependent Kinetics of Interfacial Proton-Coupled Electron Transfer. *J. Am. Chem. Soc.* **2016**, *138* (9), 3228–3234. https://doi.org/10.1021/jacs.6b00167.

(3) Berger, T.; Monllor-Satoca, D.; Jankulovska, M.; Lana-Villarreal, T.; Gomez, R. The Electrochemistry of Nanostructured Titanium Dioxide Electrodes. *ChemPhysChem* **2012**, *13* (12), 2824–2875. https://doi.org/10.1002/cphc.201200073.

(4) Fabregat-Santiago, F.; Mora-Seró, I.; Garcia-Belmonte, G.; Bisquert, J. Cyclic Voltammetry Studies of Nanoporous Semiconductors. Capacitive and Reactive Properties of Nanocrystalline TiO_2 Electrodes in Aqueous Electrolyte. *J. Phys. Chem. B* **2003**, *107* (3), 758–768. https://doi.org/10.1021/jp0265182.

(5) Rothenberger, G.; Fitzmaurice, D.; Graetzel, M. Spectroscopy of Conduction Band Electrons in Transparent Metal Oxide Semiconductor Films: Optical Determination of the Flatband Potential of Colloidal Titanium Dioxide Films. *J. Phys. Chem.* **1992**, *96* (14), 5983–5986. https://doi.org/10.1021/j100193a062.

(6) Grozovski, V.; Vesztergom, S.; Lang, G. G.; Broekmann, P. Electrochemical Hydrogen Evolution: H^+ or H_2O Reduction? A Rotating Disk Electrode Study To. *J. Electrochem. Soc.* **2017**, *164*, E3171. https://doi.org/10.1149/2.0191711jes.

(7) Lindström, H.; Södergren, S.; Solbrand, A.; Rensmo, H.; Hjelm, J.; Hagfeldt, A.; Lindquist, S.-E. Li^+ Ion Insertion in TiO_2 (Anatase). 2. Voltammetry on Nanoporous Films. *J. Phys. Chem. B* **1997**, *101* (39), 7717–7722. https://doi.org/10.1021/jp970490q.

(8) Auer, A.; Steiner, D.; Portenkirchner, E.; Kunze-Liebhäuser, J. Nonequilibrium Phase Transitions in Amorphous and Anatase TiO_2 Nanotubes. *ACS Appl. Energy Mater.* **2018**, *1* (5), 1924–1929. https://doi.org/10.1021/acsaem.7b00319.

(9) Jiang, Y.; Hall, C.; Song, N.; Lau, D.; Burr, P. A.; Patterson, R.; Wang, D.; Ouyang, Z.; Lennon, A. Evidence for Fast Lithium-Ion Diffusion and Charge-Transfer Reactions in Amorphous TiO_x Nanotubes: Insights for High-Rate Electrochemical Energy Storage. *ACS Appl. Mater. Interfaces* **2018**, *10*, 42513–42523. https://doi.org/10.1021/acsami.8b16994.

(10) Ye, J.; Shea, P.; Baumgaertel, A. C.; Bonev, S. A.; Biener, M. M.; Bagge-Hansen, M.; Wang, Y. M.; Biener, J.; Wood, B. C. Amorphization as a Pathway to Fast Charging Kinetics in Atomic Layer Deposition-Derived Titania Films for Lithium Ion Batteries. *Chem. Mater.* **2018**, *30*, 8871–8882. https://doi.org/10.1021/acs.chemmater.8b04002.

(11) Moitzheim, S.; De Gendt, S.; Vereecken, P. M. Investigation of the Li-Ion Insertion Mechanism for Amorphous and Anatase TiO_2 Thin-Films. *J. Electrochem. Soc.* **2019**, *166* (2), A1–A9. https://doi.org/10.1149/2.1091816jes.